Inversion of strong-field photoelectron spectra for molecular orbital imaging

R. Puthumpally-Joseph,[1,*] J. Viau-Trudel,[1,2] M. Peters,[3] T. T. Nguyen-Dang,[2] O. Atabek,[1] and E. Charron[1]

[1]*Institut des Sciences Moléculaires d'Orsay (ISMO), CNRS, Université Paris-Sud, Université Paris-Saclay, F-91405 Orsay, France*
[2]*Département de Chimie, Université Laval, Québec, Québec G1K 7P4, Canada*
[3]*Université de Moncton, Edmundston, New Brunswick E3V 2S8, Canada*

Imaging structures at the molecular level is a developing interdisciplinary research field that spans the boundaries of physics and chemistry. High-spatial-resolution images of molecules can be obtained with photons or ultrafast electrons. In addition, images of valence molecular orbitals can be extracted via tomographic techniques based on the coherent extreme UV radiation emitted by a molecular gas exposed to an intense ultrashort infrared laser pulse. In this paper, we demonstrate that similar information can be obtained by inverting energy-resolved photoelectron spectra using a simplified analytical model.

I. INTRODUCTION

Assessing geometric and electronic structures of molecules via different scattering techniques using x rays, ultrafast electrons, and high harmonic generations (HHG) is a hot topic of current research in molecular physics since they provide a gateway to imaging of chemical reactions in real time [1–3]. Conventional scattering techniques based on photons and electrons are able to achieve the spatial resolutions needed for imaging static molecular geometry but they lack resolution in time to give a dynamic picture. Techniques based on strong-field ionization and ultrafast lasers are promising, as they can be used to provide both subangstrom spatial and sub-femtosecond temporal resolutions [4,5] for dynamic imaging purposes. It is one of these techniques associated with strong-field ionization of molecules that is of interest in the present paper. For a thorough account of the latest trends in ultrafast molecular imaging methods, we refer the reader to Ref. [6].

The currently accepted vision of strong-field ionization is the celebrated three-step model [7,8]. When an atom or a molecule is excited with an intense infrared (IR) laser pulse, a quasistatic potential barrier is formed in the combined potential curve of the system and the field through which a bound electron can tunnel out [9]. It creates a laser-driven electron wave packet in the ionization continuum, which is driven back and forth to the parent core by the applied field. On its return to this ionic core, the electron wave packet is scattered, resulting either in elastic scattering or in inelastic collision processes such as high harmonic generation and nonsequential double ionization [10–12].

Compared to the relatively inefficient inelastic processes, elastic scattering of the ionized wave packet is the predominant outcome of recollision. It is known as laser-induced electron diffraction (LIED). Following the first theoretical discussions in 1996 [10], experimental realization of LIED in simple molecular systems was first reported in 2008 [13]. Since then, LIED has been considered a tool to study strong-field dynamics of isolated molecules.

It is well known from optical physics that a diffraction pattern can be seen as the image of an object in the reciprocal space, from which light, or an incident matter wave, has been scattered. By designing an inverse algorithm, one can reconstruct the image of that object in real space. LIED can be seen in the same perspective [10,13], but unlike traditional scattering processes, in LIED the scattering beam of electrons is extracted from the molecular system itself, acting as its own electron gun. After ionization and after an eventual recollision event, the outgoing electron wave carries information about the scattering centers. The photoelectron spectrum can thus be considered an image of the system in the reciprocal space. Given the similarity of LIED to traditional diffraction techniques, it seems potentially possible to get information about the molecule from its LIED photoelectron spectra.

It was demonstrated both theoretically and experimentally that LIED can be used for extracting structural information about the equilibrium geometry of molecules with great accuracy [14–16]. These recent experiments have motivated the development of LIED-based techniques for imaging molecular dynamics. In particular, experimental developments reported in Ref. [14] demonstrate the simultaneous measurement of both C-H and C-C bond lengths of aligned C_2H_2 using LIED spectra obtained with mid-IR laser fields. That the LIED spectral data can be inverted to retrieve precise information on the molecular geometry is not surprising, although it undoubtedly represents a huge advance in molecular physics, given that this measure can, in principle, be made on a very short time scale, allowing molecular geometry changes during a reactive collision, for example, to be followed in a time-resolved manner.

Recently, one of the key research topics in strong-field physics appeared to be the exploitation of the recollision process not only to retrieve structural or geometrical images but also to infer information on the electronic charge distribution of a molecule and even details of its field-free quantum eigenstates. These pieces of information are of great interest, especially for the understanding and the imaging of reaction dynamics, where changes in the electronic charge distribution play a major role. Achieving the required spatial and temporal resolution could provide a tool for probing the transition states of a chemical reaction, for example, by observing time-resolved deformation of the orbitals as transition states are crossed. Such a tool would also be of tremendous value to

*raiju.pj@gmail.com

image the rapid dynamics which takes place close to conical intersections [17,18].

Currently, HHG is the only strong-field process that has been explored as a tool for imaging molecular orbitals (MOs) using tomographic techniques [19], as originally demonstrated in Ref. [20]. This HHG-based orbital imaging approach involves a rather elaborated inversion procedure, requiring the HHG spectra to be recorded at various laser-molecule alignment angles, and their treatment, i.e., the inversion procedure per se, rests on a number of assumptions that are still a matter of debate.

In this paper, we propose an alternative route that can be used to extract both structural and orbital information on a molecule directly from its LIED spectra. Previously, we demonstrated how LIED signals, for a symmetric molecule such as CO_2, reflect the conservation of the nodal structure, i.e., the symmetry character, of the initial MO from which the ionized electron has been extracted. Here, we show that more detailed information on this initial orbital can be retrieved from this signal, culminating with an explicit, complete MO reconstruction procedure.

The outline of the paper is as follows. In Sec. II we briefly recall the single-active-electron (SAE) model of the CO_2 molecule as defined in the previous work and used in the present study, together with the numerical procedure for electron wave-packet calculations within this model. Then, in Sec. III, through results of numerical simulations, we illustrate the specific features of the photoelectron LIED spectrum associated with a *molecular* orbital compared to that of a typical *atomic* orbital. In Sec. IV, we derive an analytical expression of the LIED photoelectron momentum distribution, starting from formally exact integral expressions of the time-evolution operator describing the SAE dynamics. The final analytical model makes use of the strong-field approximation (SFA) and the inversion procedure used for the MO reconstruction assumes a simple LCAO expression as a guess for the initial MO. Finally in Sec. V, we demonstrate this procedure in the case of the highest-occupied molecular orbital (HOMO) of the carbon dioxide molecule. We present some examples of reconstruction and we specify the accuracy and limits of our approach. The last section gives some concluding remarks and perspectives for future work. Atomic units are used throughout the paper unless stated otherwise.

II. THEORETICAL MODEL

To demonstrate how MOs can be imaged using LIED, we consider the specific case of the symmetric, linear, carbon dioxide molecule, CO_2, one of the most studied system in strong-field physics [21–25]. It is sufficiently complex to represent an interesting test case and it is relatively simple for calculations. It enables one to demonstrate the key features of electron dynamics in the presence of intense near-IR fields [16].

The electronic dynamics induced by the field is described by the time-dependent Schrödinger equation (TDSE)

$$\hat{\mathcal{H}}(t)|\psi(t)\rangle = i\,\partial_t|\psi(t)\rangle, \quad (1)$$

where $|\psi(t)\rangle$ denotes the time-dependent electronic state of the model system constituted of the most weakly bound electron

of the molecule and

$$\hat{\mathcal{H}}(t) = -\nabla^2/2 + V(\boldsymbol{r}) - \boldsymbol{\mu}\cdot\boldsymbol{E}(t) \quad (2)$$

is its Hamiltonian in the length gauge. Here $V(\boldsymbol{r})$ is an effective field-free binding potential and $-\boldsymbol{\mu}\cdot\boldsymbol{E}(t)$ is the interaction of the active electron with the laser field. The linearly polarized electric field along $\hat{\boldsymbol{e}}_x$ is defined as

$$\boldsymbol{E}(t) = -\partial_t\,\boldsymbol{A}(t), \quad (3)$$

where $\boldsymbol{A}(t)$ is the vector potential given by

$$\boldsymbol{A}(t) = \frac{E_0}{\omega_L}\,f(t)\cos(\omega_L t + \phi)\,\hat{\boldsymbol{e}}_x\,. \quad (4)$$

ω_L is the IR career frequency and E_0 the electric-field amplitude. ϕ is the carrier-envelope phase (CEP) and

$$f(t) = \sin^2\left(\frac{\pi t}{2\tau}\right) \quad (5)$$

denotes the temporal envelope of the pulse of full width at half-maximum (FWHM) τ.

The effective multiwell potential $V(\boldsymbol{r})$ is as given in Ref. [16]. It is a soft Coulomb potential describing the attraction exerted on the single electron of the model system by screened nuclear charges with a screening factor that, for each nucleus, varies slowly with the distance separating the electron from the nuclear charge. We assume that the CO_2 molecule is prealigned along the y direction. The intense IR laser pulse given by Eq. (3) is therefore applied normal to the molecular axis. Thus the ionization and associated dynamics are assumed to take place in the plane defined by the orthogonal system of coordinates consisting of the molecular y axis and of the polarization x axis of the applied time-dependent electric field.

Figure 1(a) depicts the geometry of the system within these assumptions and shows schematically three typical ionization and recollision trajectories. The most probable recollision processes take place following a short trajectory [29], in about half an optical cycle and therefore on a time scale of the order of 1 to 3 fs for wavelengths between 800 nm and 2 μm. The electronic dynamics that takes places on this typical time scale can be separated from the nuclear dynamics, whose time scale
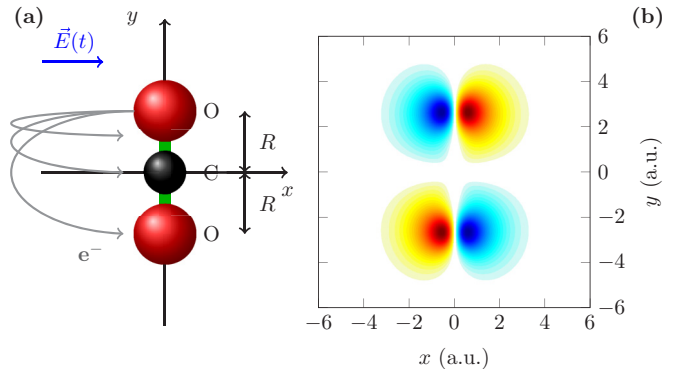

FIG. 1. (a) Model system with typical recollision trajectories. (b) Schematic of the HOMO wave function of a symmetric CO_2 molecule with CO internuclear distance $R = R_e \simeq 1.4$ Å $\simeq 2.6$ a.u. Blue, negative values; red, positive values. The wave function is antisymmetric with respect to the $x = 0$ and $y = 0$ planes.

is of the order of 15 fs for the asymmetric stretch, 25 fs for the symmetric stretch, and 60 fs for the bending modes of CO_2. We therefore consider, in a first approximation, that the nuclear motion is frozen with a fixed CO bond length R.

The TDSE, (1), describing the electronic dynamics is solved with the split-operator method [26]. The initial state is calculated using the imaginary time propagation technique [27] and the ionization and recollision events are simulated by propagating the calculated initial state during the pulse. During the interaction with the field, the asymptotic part of the wave packet is extracted and projected onto Volkov states in order to describe analytically the long-range electronic dynamics [28]. At the end of the pulse, corresponding to the time $t = t_f = 2\tau$, the asymptotic part of the wave packet is collected to obtain the energy-resolved transition amplitudes and hence the photoelectron spectrum. The entire numerical procedure is detailed in Ref. [16]. The calculated photoelectron spectrum is the laser-induced electron diffraction spectrum $\mathcal{I}(k_x, k_y)$, which gives the two-dimensional (2D) momentum distribution of the elastically scattered electron wave packets.

III. LASER-INDUCED ELECTRON DIFFRACTION SPECTRA

We discuss here the salient features of typical LIED spectra in preparation for the derivation of the inversion procedure in the next section. These spectra are calculated for the HOMO orbital of CO_2, shown in Fig. 1(b), as the initial state. We also consider the spectra associated with the ionization out of a $2p_x$ atomic orbital centered on the carbon atom. This is referred to as the atomic case.

A. Influence of the wavelength

LIED photoelectron spectra provide a picture of the momentum ($\boldsymbol{k}$) distribution of the ionized electron. A typical photoelectron spectrum $\mathcal{I}(k_x, k_y)$ obtained from the solution of the TDSE for the HOMO orbital of CO_2 at an extended geometry $R = 5$ Å is given on log scale in Fig. 2 for three wavelengths and a single-optical-cycle pulse ($2\tau = 2\pi/\omega_L$) with no CEP ($\phi = 0$). Figure 2(a) shows the spectrum at a wavelength of 800 nm, Fig. 2(b) at 1.4 μm, and Fig. 2(c) at 2.0 μm for a laser intensity of 10^{14} W/cm^2. The highest probabilities are in red and the lowest in blue.

The outermost contour of the circular shape of the spectrum is elongated along k_x, i.e., in the direction of the polarization of the field. Two successive ionization events corresponding to the maximum and minimum of $E(t)$ in this ultrashort pulse create an oscillating continuum wave packet which is ultimately driven away from the molecule. The ionization events happen along the direction of the field, giving photoelectrons with momenta distributed as shown in the figure. The circular shape corresponds to the maximum recollision energy $3.17 U_p = (k_x^2 + k_y^2)/2$, where U_p is the ponderomotive energy [29]. Since U_p is proportional to λ^2, an increase of the wavelength directly increases the size of the 2D photoelectron spectrum, as we can see in Fig. 2. Longer wavelengths thus help in making out the interference patterns of the spectrum. In the following we use the longest wavelength $\lambda = 2.0\,\mu$m.

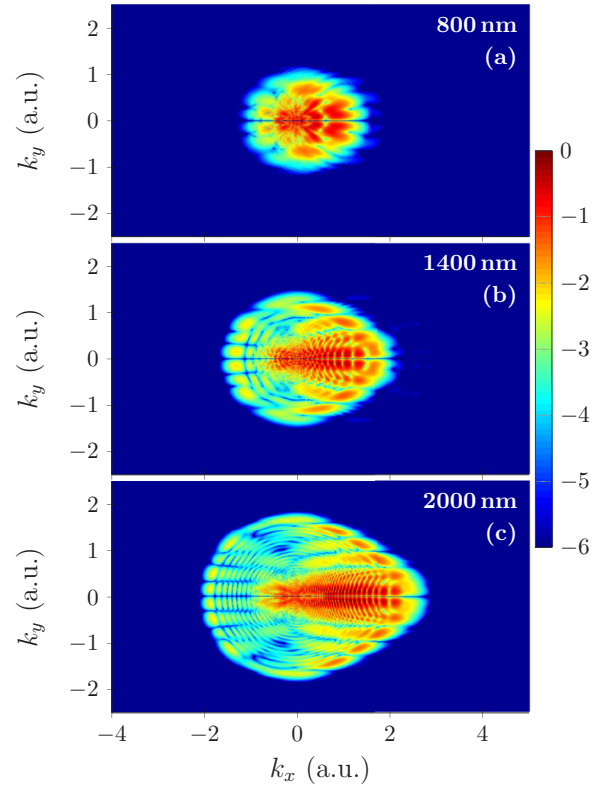FIG. 2. Normalized 2D photoelectron spectra $\mathcal{I}(k_x, k_y)$ (log scale; see color map) obtained from the HOMO of CO_2 for $R = 5$ Å when exposed to a single-optical-cycle pulse of intensity $I = 10^{14}$ W/cm^2 and zero CEP. Wavelengths used are (a) $\lambda = 800$ nm, (b) $\lambda = 1.4\,\mu$m, and (c) $\lambda = 2.0\,\mu$m.

B. Interference patterns

To analyze in detail the interference patterns which build up in the photoelectron spectra, we compare in Figs. 3(d) and 3(c) the spectrum obtained from the HOMO of CO_2 to the spectrum obtained from a $2p_x$ atomic orbital with the same ionization potential, at a wavelength of 2.0 μm. All other parameters are as in Fig. 2. Figures 3(a) and 3(b) show, respectively, the time variations of the electric field and of the total ionization probability for the atomic (solid red line) and for the molecular (dashed blue line) cases. For the atomic calculation, the parameters of the soft-core potential $V(\boldsymbol{r})$ in Eq. (2) have been modified such that the atom has the same ionization potential compared to the HOMO of CO_2, i.e., 9.2 eV at $R = 5$ Å. The electric field $E(t)$ presents two main symmetric maxima pointing in opposite directions. For both the atomic and the molecular cases, the ionization takes place in two successive bursts. The probability of ionization rises just after each maximum of the field, and the delay separating a maximum of the field and the associated ionization burst is simply related to the time necessary for the ionized wave function to reach the asymptotic region.

In the atomic photoelectron spectrum shown in Fig. 3(c) very clear ringlike structures can be seen, which come from the interference between different rescattered electron wave packets. More precisely these structures are due to the interference between long and short trajectories followed by
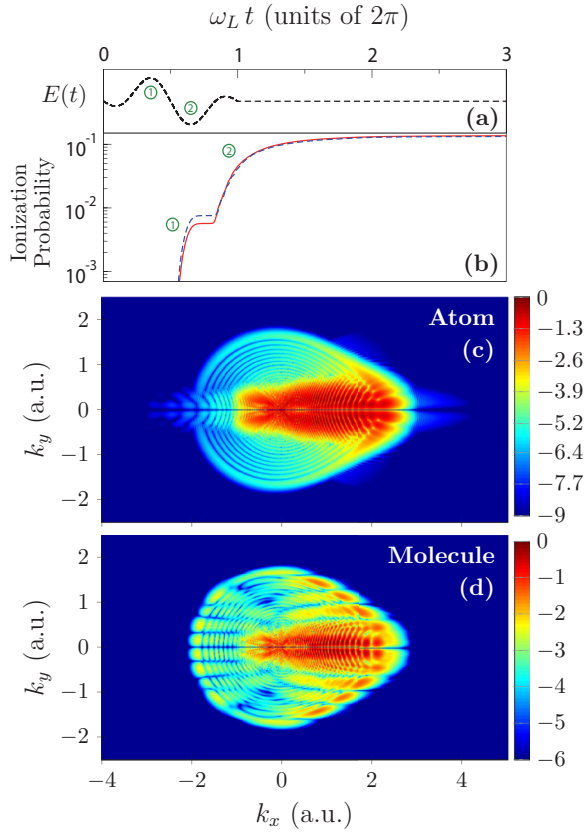
FIG. 3. (a) Normalized electric field $E(t)$ as a function of time. (b) Ionization probability as a function of time for an atom (solid red line) and a molecule (dashed blue line) with the same ionization potential, IP = 9.2 eV. (c), (d) Associated normalized 2D photoelectron spectra $\mathcal{I}(k_x, k_y)$ (log scale; see color maps) for the atom (c) and the molecule (d) at $R = 5$ Å. A single-optical-cycle pulse of intensity $I = 10^{14}$ W/cm^2 and wavelength $\lambda = 2.0$ μm is used.

recolliding electrons [30]. They have a circular shape because, for a given energy long and short trajectories accumulate a fixed phase shift which is independent of the electron emission angle.

Another interesting interference in the atomic LIED spectrum is due to the superposition of the pathways corresponding to direct ionization and to ionization preceded by recollision (i.e., to rescattering). This holographic interference of the electron wave occurs only over a window of small k_y values due to the limited spread of directly ionized electrons in the transverse direction [31–33]. It also appears mainly in the $k_x > 0$ region in Fig. 3(c) (intensely red region) due to the particular field $E(t)$ shown in Fig. 3(a), which drags the electron in the positive direction during the recollision. The associated interference patterns are relatively localized, i.e., limited in extension and are, therefore, difficult to measure in an experiment. In addition, they are seen in both the atomic and the molecular cases, as shown in the comparison with Fig. 3(d), and they are therefore not the best candidates for an analysis of the molecular structure.

There is, however, a very clear and important difference between the atomic and the molecular spectra, which lies in the
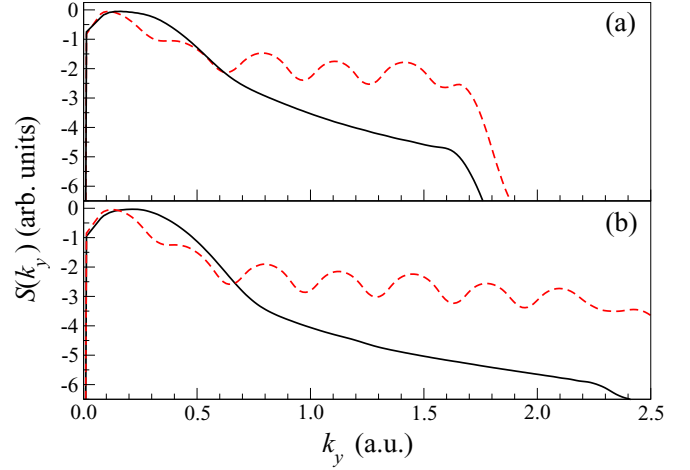

FIG. 4. Averaged 1D LIED spectra $\mathcal{S}(k_y)$ (log scale) in the atomic case (solid black line) and in the molecular case (dashed red line). (a), (b) Parameters are as in Figs. 3 and 5, respectively: Total pulse duration of (a) 1 optical cycle and (b) 3.5 optical cycles. All other parameters are identical.

k_y variation of the spectra. Indeed, of the different interference patterns seen in the molecular spectrum, a multiple-slit-like interference can be distinguished in the k_y momentum distribution. This multiple-slit-like interference pattern is due to the scattering of the electron by the multiwell ionic potential describing the interaction with the nuclei. The molecular information, including the relative position of the nuclei, is therefore mainly imprinted in the k_y momentum distribution, along the direction of the molecular axis. To get a simpler spectrum that we can more easily analyze, we average the electron signal $\mathcal{I}(k_x, k_y)$ over the k_x momentum, keeping only the k_y variation. This yields the averaged 1D LIED spectrum

$$\mathcal{S}(k_y) = \int \mathcal{I}(k_x, k_y)\, dk_x \,. \qquad (6)$$

It has been demonstrated that the bond length R can directly be measured from the fringe width seen in this 1D spectrum [16].

Two such log-scale spectra are shown in Fig. 4(a) for the cases presented in two dimensions in Figs. 3(c) and 3(d). The averaged 1D atomic spectrum is shown as the solid black line, and the molecular spectrum as the dashed red line. We clearly see strong differences in these 1D spectra, which lie both in the oscillatory behavior of the molecular spectrum and in the slower decrease (with respect to k_y) in the mean signal of the molecular spectrum compared to the atomic spectrum.

Until now, LIED spectra were calculated for a single optical cycle only. Figure 5 shows similar atomic and molecular spectra, calculated with a 3.5-optical-cycle laser pulse. Even though the pulse duration is much longer, there are only three main maxima of the electric field which contribute significantly to the ionization signal, as shown in Figs. 5(a) and 5(b). These maxima give rise to three bursts of ionization taking place in opposite directions. As a consequence, the associated 2D momentum spectra are much more symmetric with respect to $k_x = 0$ than the spectra associated with a single-cycle pulse shown in Fig. 3.
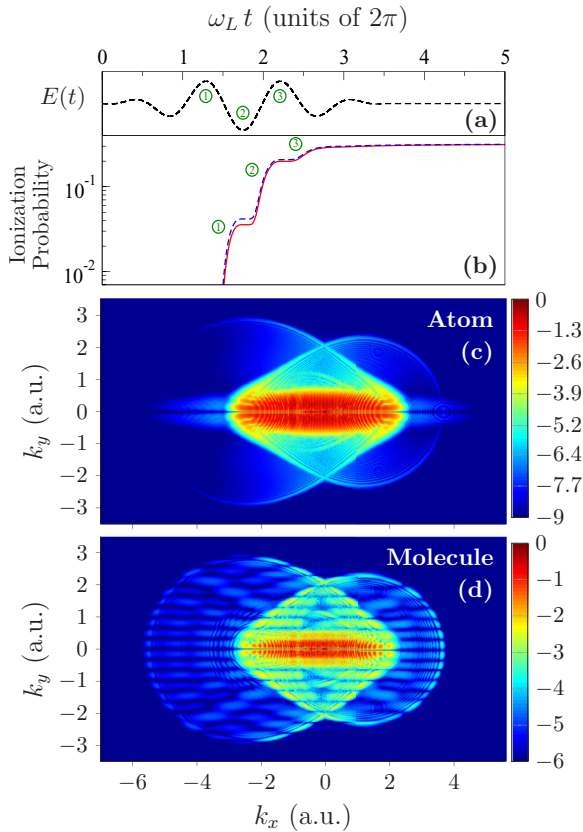
FIG. 5. (a) Normalized electric field $E(t)$ as a function of time. (b) Ionization probability as a function of time for an atom (solid red line) and a molecule (dashed blue line) with the same ionization potential, IP = 9.2 eV. (c), (d) Associated normalized 2D photoelectron spectra $\mathcal{I}(k_x,k_y)$ (log scale; see color maps) for the atom (c) and the molecule (d) at $R = 5$ Å. A 3.5-optical-cycle pulse characterized by an intensity of $I = 10^{14}$ W/cm^2 and a wavelength $\lambda = 2.0$ μm is used.

The different kinds of interference patterns discussed above are still visible. In particular, the multiple-slit-like interference seen in the k_y variation of the 2D molecular spectrum is still present. The associated k_x-averaged 1D spectra shown in Fig. 4(b) therefore show a similar behavior compared to the ultrashort single-cycle pulse. A comparison of Figs. 4(a) and 4(b) shows that the longer pulse yields a higher value of the cutoff energy. This is because the maximum value of $E(t)$ is higher for the longer pulse [see Figs. 3(a) and 5(a)]. The particular oscillatory behavior of $\mathcal{S}(k_y)$ in the molecular case in Fig. 4(b) shows that it is possible to attempt an analysis of the molecular structure from LIED spectra using few-cycle laser pulses.

C. Influence of the internuclear distance

In Fig. 6 we explore the R dependence of the LIED spectra. The intensity is 10^{14} W/cm^2 and the pulse duration is 3.5 optical cycles at the wavelength 2.0 μm. Figures 6(a)–6(c) are for $R = 2.0$ Å, $R = 3.5$ Å, and $R = 5.0$ Å, respectively. We can conclude from this figure that the interference between long and short trajectories and the interference between direct ionization and ionization preceded by recollision (rescattering
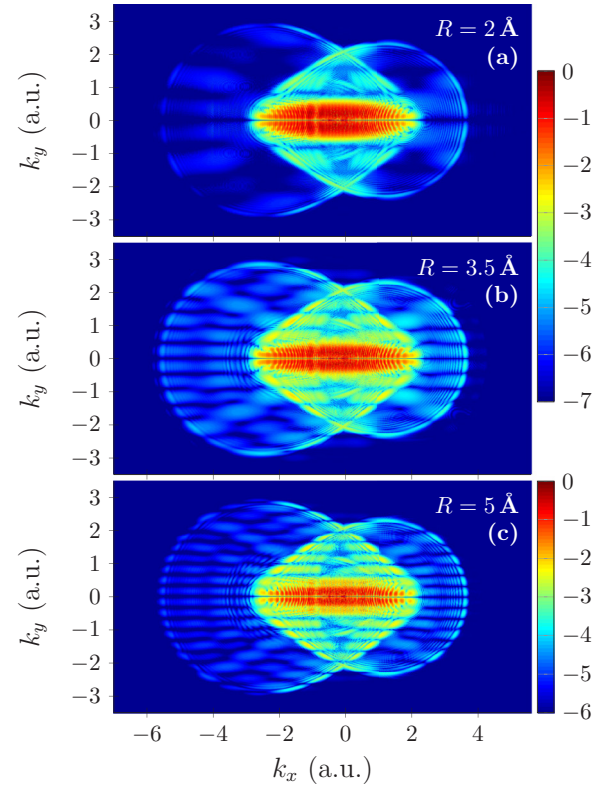

FIG. 6. R dependence of the normalized 2D photoelectron spectra $\mathcal{I}(k_x,k_y)$ (log scale; see color maps) for the CO$_2$ molecule. The intensity is $I = 10^{14}$ W/cm^2 and the pulse duration is 3.5 optical cycles. The wavelength is $\lambda = 2.0$ μm. The internuclear distance is (a) $R = 2$ Å, (b) $R = 3.5$ Å, and (c) $R = 5$ Å.

signal) are not seriously affected by a variation of the internuclear distance. On the other hand, the multiple-slit-like interference patterns seen in the k_y variation of the 2D molecular spectrum change appreciably when the internuclear distance varies.

This strong variation is confirmed by Fig. 7, which shows the associated k_x-averaged 1D LIED spectra. Figures 7(a)–7(c) are for $R = 2.0$ Å, $R = 3.5$ Å, and $R = 5.0$ Å, respectively. We see here that the analysis of the spectrum is facilitated by large internuclear distances since the oscillation period of the 1D averaged spectrum decreases with R. Indeed, it was shown in Ref. [16] that the fringe width Δk varies as π/R. This result is used in Sec. V for the reconstruction of the initial MO.

For the laser parameters used in the present calculation, i.e., $I = 10^{14}$ W/cm^2 and $\lambda = 2.0$ μm, the ponderomotive energy is $U_p = 1.38$ a.u., and, as shown in Fig. 6, the electron spectrum extends over a range of momenta of a few atomic units only, with $k_y \leqslant 2.95$ a.u. As we can already infer from Fig. 7(a) this range is not sufficient for an accurate analysis of the spectrum when $R < 3$ Å. In the following we discuss this analysis for the cases $R = 3.5$ Å and $R = 5.0$ Å. Analyzing the LIED spectra at smaller internuclear distances would require higher laser intensities or longer wavelengths.

The understanding of the LIED spectra described in detail in this section can be used for the ultimate goal of this paper: the derivation of an inversion procedure. In the next section we describe the main ingredients of an analytical model that can
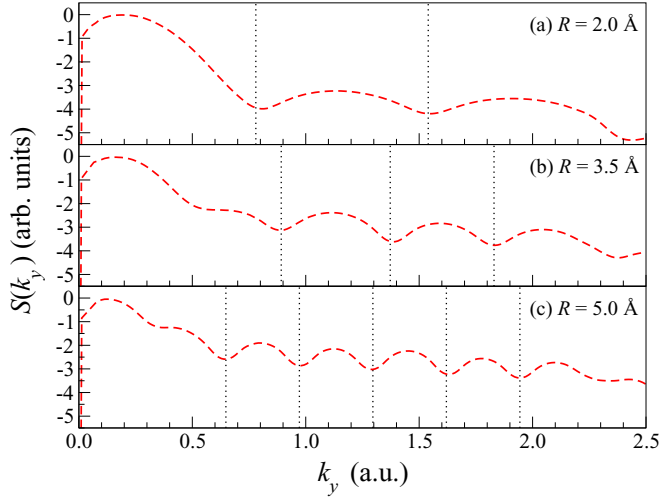
FIG. 7. R dependence of the averaged 1D LIED spectra $\mathcal{S}(k_y)$ (log scale). The internuclear distance is (a) $R = 2.0$ Å, (b) $R = 3.5$ Å, and (c) $R = 5.0$ Å. Other parameters are as in Fig. 6. Dotted vertical lines mark the regularly spaced local minima of the three spectra.

lead to the image of the MO, in the present case the HOMO, by inverting the LIED spectrum. This model is then used in the last section to analyze the spectra and to reconstruct the initial molecular orbital.

IV. THE INVERSE PROBLEM: AN ANALYTICAL MODEL

The 2D LIED spectrum $\mathcal{I}(k_x, k_y)$ calculated by solving the TDSE contains information about the molecule within the diffraction patterns, as described in Sec. III. Since this spectrum originates from the HOMO orbital of CO_2, both structural and orbital information is necessarily imprinted in it. Here the goal is to reconstruct the initial orbital from which the photoelectrons are extracted. We are thus facing what could be called an *inverse problem*, where we need a compact analytical form for the photoelectron spectra $\mathcal{S}(k_y)$ accurate enough to assess both orbital and geometrical information. This analytical form contains some parameters describing the initial state. These parameters are fitted such that the analytical form of $\mathcal{S}(k_y)$ reproduces its "exact" counterpart obtained from the solution of the TDSE. Finally, the fitted parameters are used to reconstruct the initial MO.

In general for the case discussed here, two main ingredients are necessary: (i) an approximate description of the ionization and associated dynamics that result in the photoelectron spectra and (ii) a simplified functional form for the initial state which will be used for the reconstruction. The first part is the most challenging feature of the inverse problem and is discussed in this section.

A. Description of the dynamics

1. Exact transition amplitude

The field-induced dynamics can be modeled by depicting the different steps in a recollision event [7] separately. In agreement with this mechanism describing the ionization and recollision processes, we separate the transition amplitude

$a(k_x, k_y)$ into two parts, corresponding to directly ionized electrons and to electrons ionized after a recolliding event.

If the exact solution $|\Psi(t_f)\rangle$ of the TDSE is known at the end of the pulse, at time t_f, the relevant transition amplitude for LIED can be written as

$$a(k_x, k_y) = \langle \Psi_{\boldsymbol{k}}^+ | \Psi(t_f) \rangle, \tag{7}$$

where $|\Psi_{\boldsymbol{k}}^+\rangle$ is the outgoing wave elastically scattered in the direction of the electron wave vector $\boldsymbol{k}$ for a prescribed asymptotic kinetic energy $\varepsilon_k = k^2/2$. The formal solution of the TDSE may be written at time t_f as

$$|\Psi(t_f)\rangle = \hat{U}(t_f \leftarrow 0) |\Psi(0)\rangle, \tag{8}$$

where $|\Psi(0)\rangle$ is the initial state and $\hat{U}(t \leftarrow 0)$ is the evolution operator obeying the TDSE,

$$i \, \partial_t \, \hat{U}(t \leftarrow 0) = \hat{\mathcal{H}}(t) \, \hat{U}(t \leftarrow 0). \tag{9}$$

$\hat{\mathcal{H}}(t)$ given in Eq. (2) contains both the binding and the driving potentials. Depending on the situation, one of them could be more influential than the other and could decide the outcome of the dynamical process [34].

The simplest realistic picture of strong-field ionization including the essential ingredients of tunnel ionization followed by recollision requires one to consider at least a complete optical cycle. For the derivation of the model, we therefore consider a single optical cycle of duration $t_f = 2\pi/\omega_L$. For certain times t' within this cycle, the field reaches values sufficient to trigger both tunnel ionization and the following dynamics of the wave packet, which can be represented using the exact form of the Dyson equation [35–37],

$$\hat{U}(t_f \leftarrow 0) = \hat{U}_0(t_f \leftarrow 0)$$
$$+ i \int_0^{t_f} \hat{U}(t_f \leftarrow t') \hat{\boldsymbol{\mu}} \cdot \boldsymbol{E}(t') \hat{U}_0(t' \leftarrow 0) \, dt', \tag{10}$$

where $\hat{U}_0(t \leftarrow 0)$ is the evolution operator associated with the field-free Hamiltonian

$$\hat{\mathcal{H}}_0 = -\nabla^2/2 + V(\boldsymbol{r}). \tag{11}$$

The Dyson equation, (10), is exact insofar as it involves the exact evolution operator $\hat{U}(t_f \leftarrow t')$ between the time of ionization t' and the final time t_f. During this time interval a recollision event may take place, whenever the electron wave packet propagating in the laser field comes close enough to the parent ionic core such that the Coulomb attraction starts to dominate over the driving dipole interaction. To express this idea, we then split the evolution operator $\hat{U}(t_f \leftarrow t')$, found in the integral on the right-hand side (rhs) of Eq. (10), as

$$\hat{U}(t_f \leftarrow t') = \hat{U}_v(t_f \leftarrow t') - i \int_{t'}^{t_f} \hat{U}(t_f \leftarrow t'')$$
$$\times V(\boldsymbol{r}) \hat{U}_v(t'' \leftarrow t') \, dt'', \tag{12}$$

where $\hat{U}_v$ is the evolution operator associated with the Volkov Hamiltonian [36,38]

$$\hat{\mathcal{H}}_v(t) = -\nabla^2/2 - \hat{\boldsymbol{\mu}} \cdot \boldsymbol{E}(t). \tag{13}$$

The Volkov evolution operator $\hat{U}_v(t_2 \leftarrow t_1)$ can be formally written as

$$\hat{U}_v(t_2 \leftarrow t_1) = \int d\boldsymbol{k} \left|\Phi_{\boldsymbol{k}}^v(t_2)\right\rangle\!\left\langle\Phi_{\boldsymbol{k}}^v(t_1)\right|, \qquad (14)$$

where

$$\Phi_{\boldsymbol{k}}^v(\boldsymbol{r},t) = \frac{e^{i\,[\boldsymbol{k}+\boldsymbol{A}(t)]\cdot\boldsymbol{r} - i\,S(\boldsymbol{k},t)}}{2\pi}, \qquad (15)$$

$S(\boldsymbol{k},t)$ being the classical action

$$S(\boldsymbol{k},t) = \frac{1}{2}\int_0^t [\boldsymbol{k} + \boldsymbol{A}(\tau)]^2\,d\tau\,. \qquad (16)$$

Substituting Eq. (12) into Eq. (10) we get

$$\hat{U}(t_f \leftarrow 0) = \hat{U}_0(t_f) + \hat{U}_d(t_f) + \hat{U}_r(t_f), \qquad (17)$$

with the following definitions:

$$\hat{U}_0(t_f) = \exp(-i\,\hat{\mathcal{H}}_0\,t_f), \qquad (18\text{a})$$

$$\hat{U}_d(t_f) = i\int_0^{t_f} dt'\,\mathcal{D}(t_f,t'), \qquad (18\text{b})$$

$$\hat{U}_r(t_f) = \int_0^{t_f} dt'\int_{t'}^{t_f} dt''\,\hat{U}(t_f \leftarrow t'')\,V(\boldsymbol{r})\,\mathcal{D}(t'',t'), \quad (18\text{c})$$

and

$$\mathcal{D}(t_2,t_1) = \hat{U}_v(t_2 \leftarrow t_1)\,\hat{\boldsymbol{\mu}}\cdot\boldsymbol{E}(t_1)\,\hat{U}_0(t_1 \leftarrow 0)\,. \qquad (19)$$

Among the three terms composing $\hat{U}(t_f \leftarrow 0)$ in Eq. (17), $\hat{U}_d(t_f)$ is responsible for direct ionization, whereas $\hat{U}_r(t_f)$ includes recollision. It is to be stressed that Eq. (17), with the definitions given in Eqs. (18) and (19), is still exact. This type of Dyson expansion could be iterated by considering multiple ionization and higher order recollisions. In the present simplified model we stop at this second-order decomposition.

Now, using these equations, we can split the ionization amplitude into two contributions,

$$a(k_x,k_y) = a_d(k_x,k_y) + a_r(k_x,k_y), \qquad (20)$$

with

$$a_d(k_x,k_y) = \langle\Psi_{\boldsymbol{k}}^+|\,\hat{U}_d(t_f)\,|\Psi(0)\rangle \qquad (21)$$

and

$$a_r(k_x,k_y) = \langle\Psi_{\boldsymbol{k}}^+|\,\hat{U}_r(t_f)\,|\Psi(0)\rangle\,. \qquad (22)$$

Equation (21) gives the transition amplitude associated with direct ionization, while Eq. (22) gives the transition amplitude associated with ionization preceded by recollision. Hence, the 2D LIED spectrum can be written as

$$\mathcal{I}(k_x,k_y) = |a_d(k_x,k_y) + a_r(k_x,k_y)|^2, \qquad (23)$$

an expression which shows clearly the appearance of an interference between the direct and the recolliding ionization pathways. Note that such an expression is common when describing strong-field ionization using a SFA approach [39].

2. Approximate transition amplitude

Evaluating the direct ionization amplitude $a_d(k_x,k_y)$ is relatively easy compared to the recollision amplitude $a_r(k_x,k_y)$

because of the appearance of $\hat{U}(t_f \leftarrow t'')$ in the expression of $\hat{U}_r(t_f)$. To make this evaluation tractable, we use the strong-field approximation [37,40], and we replace $\hat{U}(t_f \leftarrow t'')$ with the Volkov evolution operator $\hat{U}_v(t_f \leftarrow t'')$, with

$$\hat{U}_r(t_f) \simeq \int_0^{t_f} dt'\int_{t'}^{t_f} dt''\,\hat{U}_v(t_f \leftarrow t'')\,V(\boldsymbol{r})\,\mathcal{D}(t'',t')\,. \quad (24)$$

Replacing $\hat{U}(t_f \leftarrow t'')$ with $\hat{U}_v(t_f \leftarrow t'')$ in Eq. (24) means that after the first recollision event, we neglect the Coulomb force compared to the interacting IR field, an approximation valid in the asymptotic region, where the Coulomb interaction is negligible.

As the second step in simplifying the model, the outgoing waves $|\Psi_{\boldsymbol{k}}^+\rangle$ are approximated by plane waves $|\Phi_{\boldsymbol{k}}^{\text{pw}}\rangle$. This approximation is justified asymptotically. Within these approximations we obtain

$$a_d(k_x,k_y) \simeq i\int_0^{t_f} dt'\,e^{-i\bar{S}_1}\left\langle\Phi_{\boldsymbol{k}'}^{\text{pw}}\big|\hat{\boldsymbol{\mu}}\cdot\boldsymbol{E}(t')\,|\Psi(0)\rangle\right. \qquad (25)$$

and

$$a_r(k_x,k_y) \simeq \int_0^{t_f} E(t')dt'\int_{t'}^{t_f} dt''\,e^{-i\bar{S}_2}\langle\Phi_{\boldsymbol{k}''}^{\text{pw}}\big|V(\boldsymbol{r})|\Psi_r\rangle, \quad (26)$$

where

$$\bar{S}_1 = \frac{1}{2}\int_{t'}^{t_f}[\boldsymbol{k}+\boldsymbol{A}(\tau)]^2 d\tau - I_p\,t', \qquad (27\text{a})$$

$$\boldsymbol{k}' = \boldsymbol{k} + \boldsymbol{A}(t'), \qquad (27\text{b})$$

$$\bar{S}_2 = \frac{1}{2}\int_{t''}^{t_f}[\boldsymbol{k}+\boldsymbol{A}(\tau)]^2 d\tau - I_p\,t', \qquad (27\text{c})$$

$$\boldsymbol{k}'' = \boldsymbol{k} + \boldsymbol{A}(t''), \qquad (27\text{d})$$

$$|\Psi_r\rangle = \hat{U}_v(t'' \leftarrow t')\,x\,|\Psi(0)\rangle\,. \qquad (27\text{e})$$

In Sec. III, it has been noted that the most interesting features of the photoelectron spectrum lie in the high-momentum (k_y) part of the 1D averaged spectra. This is because these electrons are characterized by de Broglie wavelengths short enough to resolve subangstrom spatial scales. Thus, describing the low-energy part of the spectrum and the parallel momentum (k_x) distribution of the photoelectrons accurately is not essential. It has also been shown that high energies are reached by electrons ionized around a maximum of the field and hence around a minimum of the potential vector [7,41]. Thus $\boldsymbol{A}(t')$ can be neglected in Eq. (27b). In addition, electrons with high kinetic energies mainly recollide with the ionic core at a minimum of the field, corresponding to a maximum of the vector potential [7,41]. In Eq. (27d) we therefore use $\boldsymbol{A}(t'') \simeq \pm E_0/\omega_L\,\hat{\boldsymbol{x}}$. The potential vector $\boldsymbol{A}(t'')$ therefore induces a strong shift of the parallel component k_x of the electron momentum. In practice, this shift is of no significance in the present approach, since it will be averaged out in the calculation of Eq. (6) and we therefore do not take it into account in the following.

Within these approximations and to avoid discrepancies between the SFA spectrum and the spectrum obtained from the solution of the TDSE, one should restrict the analysis of the 1D averaged signal to the highest k_y momentum components only. The interest of this severe approximation lies, however, in the

fact that it simplifies the model by allowing the separation of the temporal from the spatial integrals involved in Eq. (25). Thus, for the direct ionization amplitudes, one has

$$a_d(k_x, k_y) \simeq A_d \left\langle \Phi_{\boldsymbol{k}}^{\mathrm{pw}} \right| x \left| \Psi(0) \right\rangle, \qquad (28)$$

where

$$A_d = i \int_0^{t_f} E(t') \, e^{-i \bar{S}_1} \, dt' \,. \qquad (29)$$

Similarly, the recollision amplitude becomes

$$a_r(k_x, k_y) \simeq \int_0^{t_f} E(t') dt' \int_{t'}^{t_f} dt'' \, e^{-i \bar{S}_2} \left\langle \Phi_{\boldsymbol{k}}^{\mathrm{pw}} \right| V(\boldsymbol{r}) | \Psi_r \rangle. \quad (30)$$

Using the closure property of the plane-wave basis set one obtains

$$|\Psi_r\rangle = \int d\boldsymbol{k}' e^{-ik'^2 \Delta t/2} \left\langle \Phi_{\boldsymbol{k}'}^{\mathrm{pw}} \right| x | \Psi(0) \rangle \left| \Phi_{\boldsymbol{k}'}^{\mathrm{pw}} \right\rangle, \qquad (31)$$

where $\Delta t = t'' - t' \simeq 0.7 \, (2\pi/\omega_L)$ is the mean time during which the electron wave packet propagates in the continuum [7,41]. The temporal and spatial integrals can thus be separated in expression (30) of the recollision amplitude as

$$a_r(k_x, k_y) \simeq A_r \left\langle \Phi_{\boldsymbol{k}}^{\mathrm{pw}} \right| V(\boldsymbol{r}) | \Psi_r \rangle, \qquad (32)$$

where

$$A_r = \int_0^{t_f} dt' \int_{t'}^{t_f} dt'' \, E(t') \, e^{-i \bar{S}_2} \,. \qquad (33)$$

Finally, the approximate transition amplitude is given by

$$a(k_x, k_y) \simeq A_d \left\langle \Phi_{\boldsymbol{k}}^{\mathrm{pw}} \right| x | \Psi(0) \rangle + A_r \left\langle \Phi_{\boldsymbol{k}}^{\mathrm{pw}} \right| V(\boldsymbol{r}) | \Psi_r \rangle. \quad (34)$$

This equation has to be developed on a suitable basis of initial states for the final analytical form of the LIED spectra.

B. Initial molecular wave function

Equation (34) expresses the ionization amplitude as the sum of two terms, each written in the form of a product of spatial and temporal integrals. The first term is associated with direct ionization, and the second with recollision events. As we see from the LIED spectra, the information we are interested in is encoded in the spatial integrals. Thus in the following discussion, the temporal integrals A_d and A_r are taken as adjustable coefficients in order to match the approximate spectrum with the calculated spectrum.

To proceed further with the evaluation of the spatial integrals, we need to specify the initial wave function $\Psi(\boldsymbol{r}, 0) = \langle \boldsymbol{r} | \Psi(0) \rangle$. Insofar as the SAE method is valid, this initial wave function is a molecular orbital. In quantum chemistry, this is usually expressed as a linear combination of atomic orbitals (LCAO method) and there are many basis set ansatzes for representing localized atomic wave functions. Here the initial HOMO orbital is taken as an antisymmetric linear combination of $2p_x$ atomic orbitals [see Fig. 1(b)]:

$$\Psi(\boldsymbol{r}, 0) = \Phi_{2p_x}(\boldsymbol{r} + \boldsymbol{R}) - \Phi_{2p_x}(\boldsymbol{r} - \boldsymbol{R}) \qquad (35a)$$

$$= \Phi_{2p_x}^-(\boldsymbol{r}) - \Phi_{2p_x}^+(\boldsymbol{r}) \,. \qquad (35b)$$
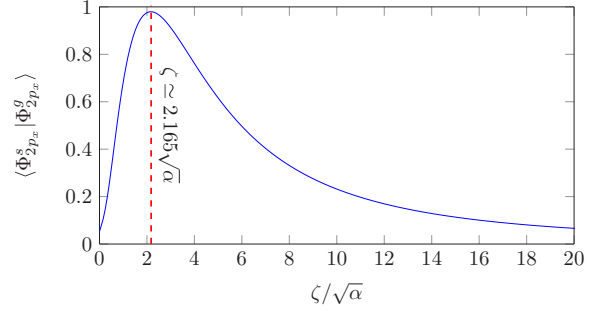

FIG. 8. Overlap (linear scale) between the Gaussian-type, (37), and the Slater-type, (36), orbitals used in the present study as a function of the dimensionless ratio $\zeta/\sqrt{\alpha}$ (see text for details).

Ideally one would choose for $\Phi_{2p_x}(\boldsymbol{r})$ a Slater-type orbital of the form

$$\Phi_{2p_x}^s(\boldsymbol{r}) = \mathcal{N}_s \, x \, e^{-\zeta r}, \quad r = (x^2 + y^2)^{1/2}, \qquad (36)$$

with the normalization factor $\mathcal{N}_s = \zeta^2 \sqrt{8/3\pi}$ in two dimensions, where ζ is the Slater exponent. This analytical form, once introduced in Eq. (35b), is a reasonable candidate for representing the HOMO orbital, but an important disadvantage then lies in the difficulty of evaluating multicenter integrals such as the recolliding integral of Eq. (34). It appears that this difficulty can be removed if the Slater orbital, (36), is replaced by a Gaussian-type orbital of the form

$$\Phi_{2p_x}^g(\boldsymbol{r}) = \mathcal{N}_g \, r \cos \theta_r \, e^{-\alpha r^2}, \qquad (37)$$

with the normalization factor $\mathcal{N}_g = \alpha \sqrt{8/\pi}$, where α is the Gaussian exponent. Actually, the Gaussian function, (37), can be approximated to the Slater orbital (36) with the appropriate choice of α.

Figure 8 shows the overlap between the wave functions (37) and (36) as a function of the dimensionless ratio $\zeta/\sqrt{\alpha}$. It is clear that for $\zeta \simeq 2.165 \sqrt{\alpha}$, the Slater and Gaussian orbitals are very similar, with an overlap of about 98%. In the following, for evaluation of the integrals, we use Gaussian-type atomic orbitals, but for reconstruction of the initial molecular state we use Slater-type orbitals whose sizes are defined from the optimal ratio $\zeta/\sqrt{\alpha} = 2.165$.

C. Approximate 1D photoelectron spectrum

The expression for the approximate transition amplitude $a(k_x, k_y)$ given in Eq. (34) can now be evaluated for the initial HOMO wave function given in Eq. (35b) as

$$a(k_x, k_y) = A_d \big[\left\langle \Phi_{\boldsymbol{k}}^{\mathrm{pw}} \right| x \left| \Phi_{2p_x}^- \right\rangle - \left\langle \Phi_{\boldsymbol{k}}^{\mathrm{pw}} \right| x \left| \Phi_{2p_x}^+ \right\rangle \big]$$
$$+ A_r \big[\left\langle \Phi_{\boldsymbol{k}}^{\mathrm{pw}} \right| V \left| \Phi_{\mathrm{rec}}^- \right\rangle - \left\langle \Phi_{\boldsymbol{k}}^{\mathrm{pw}} \right| V \left| \Phi_{\mathrm{rec}}^+ \right\rangle \big], \quad (38)$$

where $|\Phi_{\mathrm{rec}}^\pm\rangle$ denotes

$$|\Phi_{\mathrm{rec}}^\pm\rangle = \int d\boldsymbol{k}' e^{-ik'^2 \Delta t/2} \left\langle \Phi_{\boldsymbol{k}'}^{\mathrm{pw}} \right| x \left| \Phi_{2p_x}^\pm \right\rangle \left| \Phi_{\boldsymbol{k}'}^{\mathrm{pw}} \right\rangle. \qquad (39)$$

The first two integrals in Eq. (38) represent direct ionization from displaced (oxygen $2p_x$) orbitals and the last two represent the ionization amplitudes after a recollision event. The two integrals associated with direct ionization amplitudes are

just Fourier transforms of products of the dipole operator x with displaced $2p_x$ orbitals. In momentum space, this spatial translation becomes a simple phase shift of the form $\exp[\pm i k_y R]$ of the Fourier transform signal of $\Phi_{2p_x}^\pm$. Taking this simplification into account, Eq. (38) can be reduced to

$$a(k_x,k_y) = A_d \sin(k_y R) \langle \Phi_k^{pw} | x | \Phi_{2p_x} \rangle$$
$$+ A_r \left[\langle \Phi_k^{pw} | V | \Phi_{rec}^- \rangle - \langle \Phi_k^{pw} | V | \Phi_{rec}^+ \rangle \right]. \quad (40)$$

Evaluation of the direct ionization amplitude using a Gaussian-type orbital yields

$$a_d(k_x,k_y) = A_d \sin(k_y R)\left(k_x^2 - 2\alpha\right) e^{-\frac{k_x^2+k_y^2}{4\alpha}}, \quad (41)$$

provided that A_d accounts for all constant factors.

Calculation of the recollision amplitude $a_r(k_x,k_y)$ is more involved since it requires the knowledge of the functional form of the recolliding wave functions $\Phi_{rec}^\pm(\vec{r})$. Using a Gaussian-type orbital Φ_{2p_x} located at the origin for the initial state, we obtain

$$\Phi_{rec}^0(r) \propto \frac{\alpha - i\beta - 2\beta^2 x^2}{(\alpha - i\beta)^3} e^{i\gamma r^2}, \quad (42)$$

where $\gamma = \alpha\beta/(\alpha - i\beta)$ and $\beta = 1/(2\Delta t)$. The wave functions $\Phi_{rec}^\pm(r)$ are identical to $\Phi_{rec}^0(r)$ except for a phase shift, so that the corresponding recollision wave functions are given by

$$\Phi_{rec}^-(r) = e^{i\gamma R^2} e^{+i2y\gamma R} \Phi_{rec}^0(r), \quad (43a)$$

$$\Phi_{rec}^+(r) = e^{i\gamma R^2} e^{-i2y\gamma R} \Phi_{rec}^0(r). \quad (43b)$$

In the near IR ($\lambda = 800$ nm to 2.5 μm) parameter β of Eq. (42) is in the range 10^{-2} to 10^{-3} a.u. In comparison, the Gaussian orbital exponent α is usually of the order of 1 a.u. These orders of magnitudes can be used in order to simplify further the expression of the ionization amplitude.

Since the binding potential $V(r)$ is characterized by three attractive centers, the recollision amplitude $a_r(k_x,k_y)$ [second part on the rhs of Eq. (40)] contains, for the HOMO of CO_2, six integrals. Indeed, from the HOMO, ionization may originate from any of the two oxygen atoms and recollision may take place on any of the three atoms. Fortunately, these six integrals are similar. In the case of the HOMO, the electron wave packet is launched from both of the oxygen atoms labeled O_1 and O_2 in Fig. 1. Upon recollision, the contribution from the first oxygen atom O_1 will scatter from the parent atom O_1 itself as well as from the two neighboring atoms: from the carbon atom C and from the second oxygen atom O_2. This part of the rescattering amplitude, shown in Fig. 1, can be written as

$$a_r^{O_1}(k_x,k_y) = \langle \Phi_k^{pw} | V | \Phi_{rec}^+ \rangle, \quad (44)$$

where the three-center potential V, supposed to be of a Coulomb form, is given by

$$V(r) = -\frac{q_O}{|r+R|} - \frac{q_C}{|r|} - \frac{q_O}{|r-R|}. \quad (45)$$

What matters most for the recollision is the scattering taking place in the vicinity of Coulombic cores. At first order near the singularities of the potential wells, i.e., for $x \to 0$ and $y \to \{-R, 0, R\}$, and taking into account Eqs. (42) and (43),

the above integral can be reduced to

$$a_r^{O_1}(k_x,k_y) \propto \frac{-e^{ik_y R} - e^{i\beta R^2} - e^{-ik_y R} e^{i\beta 4R^2}}{|k_y|}. \quad (46)$$

Similarly, for the wave packet originating from the second oxygen atom, we obtain

$$a_r^{O_2}(k_x,k_y) = \langle \Phi_k^{pw} | V | \Phi_{rec}^- \rangle$$
$$\propto \frac{e^{-ik_y R} + e^{i\beta R^2} + e^{ik_y R} e^{i\beta 4R^2}}{|k_y|}. \quad (47)$$

Finally, the total recollision amplitude is

$$a_r(k_x,k_y) = A_r \frac{1 - e^{i4\beta R^2}}{|k_y|} \sin(k_y R). \quad (48)$$

Combining Eqs. (41) and (48) we obtain the 2D transition amplitude. The transition probability is the square modulus of this transition amplitude. Finally, averaging over the parallel momentum component k_x, the 1D spectrum is written as

$$S(k_y) = \left(|A_d|^2 e^{-\frac{k_y^2}{2\alpha}} + \frac{|A_r|^2}{k_y^2} \right) \sin^2(k_y R). \quad (49)$$

Again, A_d and A_r account here for all constant factors. Eq. (49) is the compact analytical form we use in the next section for our inversion procedure.

V. RESULTS: RECONSTRUCTION OF ORBITALS

Equation (49) is the final result we intended to derive for solving the inverse problem. Taking $|A_d|$, $|A_r|$, α, and R as four independent adjustment variables, this expression can be compared with 1D averaged LIED spectra calculated from the solution of the TDSE. In general, the model can be used for any internuclear distances of the CO_2 molecule. However, as discussed previously, with the particular laser parameters chosen in the present study our model is not expected to perform well for small values of R. We thus chose only two cases for this comparison: $R = 3.5$ Å and $R = 5.0$ Å.

To ease the multiparameter fitting procedure, it is well known that the search for the best fit should start from a good-guess value. Here the range of the parameter R can be obtained easily from the spectrum itself by measuring the fringe width $\Delta k = \pi/R$ as discussed in Ref. [16]. Thus we are left with three completely unknown parameters and one partially known parameter. The fitting process is performed here using the well-known Levenberg-Marquardt algorithm [42], because of its robustness for finding the best possible solutions even if the procedure starts with initial guess values relatively far from the final one.

The fitting process is performed on the high-kinetic-energy part of the spectra. The highest accessible kinetic energy and hence the highest momentum component k_y^{max} are defined by the cutoff energy $3.17 U_p$, which is fixed by the laser parameters used in the calculation or experiment. In order to obtain reliable values for the parameters, the fitting process must be repeated several times. This is done by varying the lower limit of the kinetic momentum k_y^{min} taken into account, between 1.15 and 1.25 a.u. in the present calculation.

TABLE I. Fitted values of the parameters involved in the SFA analytical model of Eq. (49).

	A_d (a.u.)	A_r (a.u)	R (Å)	α (a.u.)
	0.00478	0.000808	3.628	0.535
	0.00506	0.000720	3.616	0.516
$R = 3.5$ Å	0.00513	0.000634	3.624	0.527
	0.00405	0.001087	3.619	0.520
Average	0.00476	0.000812	3.622	0.525
	0.0157	0.00385	5.141	0.676
$R = 5.0$ Å	0.0121	0.00639	5.141	0.625
	0.0137	0.00507	5.142	0.657
	0.0145	0.00452	5.142	0.669
Average	0.0140	0.00496	5.142	0.657

Values of the relevant parameters obtained for four lower limits are listed in Table I. The values obtained for the internuclear distance R are very stable and accurate. In addition, the values obtained for the orbital exponent α are relatively stable. Since these two parameters are the ingredients used to reconstruct the molecular orbital, (35b), they will lead to a very similar orbital, whatever the other parameters chosen in Table I. In practice, we average over several fits in order to extract these parameters (see Table I).

Typical numerical and model 1D LIED spectra are shown in Fig. 9, for $R = 3.5$ Å [Fig. 9(a)] and $R = 5.0$ Å [Fig. 9(b)]. Numerical spectra $\mathcal{S}(k_y)$ obtained by solving the TDSE are shown as solid blue curves and fitted (model) spectra are shown as dashed red curves, as a function of k_y. As is apparent in the figure, the model and the numerical calculations fit well. For both cases considered here, the relative errors in the retrieved internuclear distances are of the order of 3%: We obtained
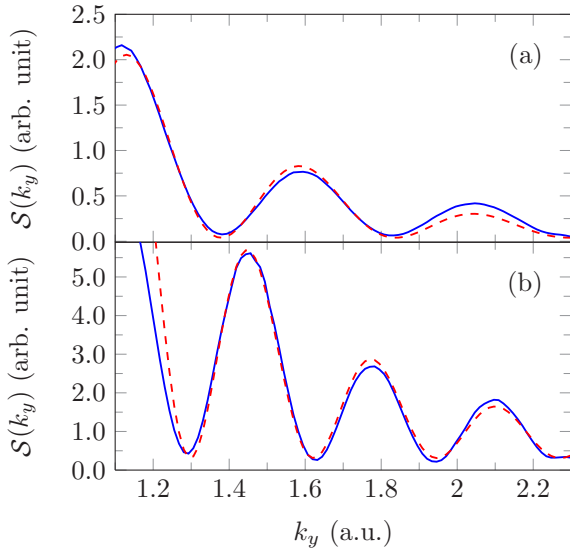

FIG. 9. One-dimensional averaged LIED spectra $\mathcal{S}(k_y)$ (linear scale). Solid blue lines are spectra calculated using the time-dependent Schrödinger equation and dashed red lines show the results of the best fits using the analytical SFA model. (a) $R = 3.5$ Å and (b) $R = 5.0$ Å.
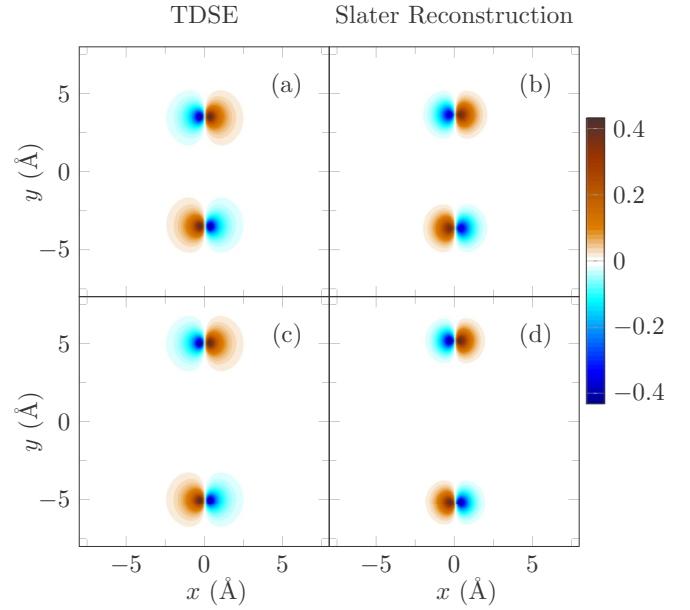

FIG. 10. (a), (c) Initial wave functions used for the TDSE calculation with $R = 3.5$ Å (a) and $R = 5.0$ Å (c) (linear scale; see color map). (b), (d) Associated reconstructed molecular orbitals (linear scale; see color map).

$R = 3.62$ Å instead of 3.50 Å and $R = 5.14$ Å instead of 5.00 Å (see averaged R values in Table I).

Taking the average values of the fitted internuclear distances R and Gaussian exponents α we can reconstruct the initial state used to derive Eq. (49). Finally, as discussed in Sec. IV B, this initial state can also be given in terms of Slater-type orbitals. These functions will give the best possible simple form of the initial state. Reconstructed approximate Slater forms of the initial states are shown in Fig. 10. Figures 10(a) and 10(c) show the initial states used in the TDSE calculation for $R = 3.5$ Å and $R = 5.0$ Å, respectively. Figures 10(b) and 10(d) are the corresponding reconstructed MOs.

The overlap between the reconstructed orbital and the initial state used in the numerical TDSE calculations is higher than 96%: 96.3% for $R = 3.5$ Å and 97.2% for $R = 5.0$ Å. This reconstruction shows that for large internuclear distances LIED techniques could be used to image MOs with a rather good accuracy using a simple multiparameter fitting procedure.

It is also possible to depict the discrepancy in the reconstructed orbitals caused by the inaccuracies in R and α by plotting the difference between the exact and the reconstructed orbitals. These differences are shown in Fig. 11 using the same color code as in Fig. 10, for $R = 3.5$ Å [Fig. 11(a)] and $R = 5.0$ Å [Fig. 11(b)]. The discrepancy shown in this figure is due to the combined errors in the reconstructed values of both the orbital exponent α and the internuclear distance R.

Any error in the internuclear distance R would be crucial since it would cause a significant mismatch in the location of the reconstructed orbital. Here, since the fitted value of R is very close to its exact value, this problem does not appear.

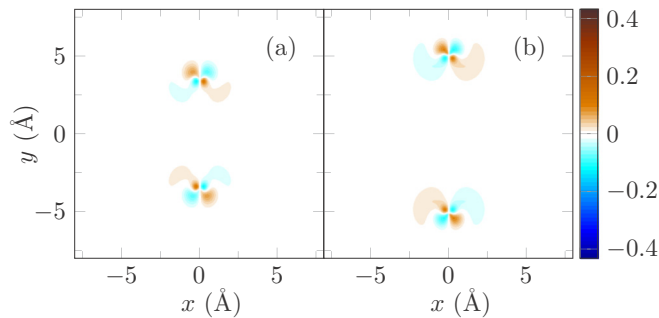A small error in the orbital exponent α is, on the other hand, not as crucial since the overlap between the exact wave

FIG. 11. Difference between the initial states and their reconstructions (linear scale; see color map). (a) $R = 3.5$ Å and (b) $R = 5.0$ Å. The color map used here is the same as that in Fig. 10.

function and the reconstructed orbital varies smoothly with α. We have calculated the optimal α values for our exact initial states by computing the overlap between the initial state and the LCAO form we have adopted in this study. We have obtained $\alpha_{\text{opt}} = 0.624$ a.u. for $R = 3.5$ Å and $\alpha_{\text{opt}} = 0.626$ a.u. for $R = 5.0$ Å. The relative errors in the fitted values of α are therefore of the order of 16% for $R = 3.5$ Å and 5% for $R = 5.0$ Å. We again see here that our inversion procedure is more accurate for the largest internuclear distance.

Being a model developed using a single-active-electron approximation, analyzing LIED processes with multielectron ionization channels may reveal additional discrepancies in the retrieved values of the parameters. One of the main problems with including interactions between electrons is the difficulty of solving such situations analytically. Aiming for a compact analytical form given with a relatively small number of fitting parameters, an extension of the model beyond the SAE approximation is far from trivial in the spirit of an inverse problem.

Other approximations could be relaxed more easily. For example, higher order processes of recollision events can be included in the picture by applying the SFA to the desired higher order terms. This may improve the model, but to our best understanding, the second-order development used here retains the main elements necessary for an accurate reconstruction procedure for linear molecules with large internuclear distances ($R > 3$ Å).

The inverse problem discussed in this paper in the case of the HOMO orbital of the CO_2 molecule can be relatively easily extended to the deeper HOMO-1 orbital by modifying the analytical model slightly. In this case, the atomic orbitals

of the three composite atoms have a significant overlap and form a symmetric MO. But the relative contributions of the C and O atoms are different. This gives an additional parameter which should be introduced into the model. This additional parameter would also have to be retrieved by an inversion procedure. It should also be relatively easy to make some other simple modifications to the analytical model to treat other linear molecules.

VI. CONCLUSION

In this paper, we discuss some possibilities for imaging molecular orbitals (MOs) offered by laser-induced electron diffraction following the strong-field ionization of a prealigned linear molecule. The problem is discussed in detail for the HOMO orbital of the carbon dioxide molecule.

The system is described theoretically in the framework of a single active electron model. The strong field photoelectron spectra are obtained by solving the time-dependent Schrödinger equation (TDSE) for different initial internuclear distances. An approximate, but compact analytical model is also developed for these photoelectron spectra using three classes of approximations: (i) the single-active-electron approximation, (ii) the strong-field approximation, and (iii) an approximate LCAO ansatz for the initial MO.

This analytical model contains some parameters which are fitted by comparison with the TDSE results. This fitting procedure allows for the extraction of the internuclear distance and the corresponding Slater-type orbital exponents. The initial ansatz for the MO is then reconstructed with these parameters, providing an accurate representation of the initial state used in the TDSE, with an overlap which is higher than 96%.

This approach can be effectively used for the reconstruction of the HOMO with a good accuracy. It should be possible to extend this model to other initial orbitals and to other linear molecules. In the future, the inclusion of the nuclear dynamics could enable this model to image reaction dynamics such as the photodissociation of linear molecules.

[1] M. P. Minitti, J. M. Budarz, A. Kirrander, J. S. Robinson, D. Ratner, T. J. Lane, D. Zhu, J. M. Glownia, M. Kozina, H. T. Lemke, M. Sikorski, Y. Feng, S. Nelson, K. Saita, B. Stankus, T. Northey, J. B. Hastings, and P. M. Weber, Phys. Rev. Lett. **114**, 255501 (2015).

[2] C. J. Hensley, J. Yang, and M. Centurion, Phys. Rev. Lett. **109**, 133202 (2012).

[3] S. P. Weathersby, G. Brown, M. Centurion, T. F. Chase, R. Coffee, J. Corbett, J. P. Eichner, J. C. Frisch, A. R. Fry, M. Gühr, N. Hartmann, C. Hast, R. Hettel, R. K. Jobe, E. N. Jongewaard,

J. R. Lewandowski, R. K. Li, A. M. Lindenberg, I. Makasyuk, J. E. May, D. McCormick, M. N. Nguyen, A. H. Reid, X. Shen, K. Sokolowski-Tinten, T. Vecchione, S. L. Vetter, J. Wu, J. Yang, H. A. Dürr, and X. J. Wang, Rev. Sci. Instrum. **86**, 073702 (2015).

[4] F. Calegari, G. Sansone, S. Stagira, C. Vozzi, and M. Nisoli, J. Phys. B: At. Mol. Opt. Phys. **49**, 062001 (2016).

[5] T. Brabec and F. Krausz, Rev. Mod. Phys. **72**, 545 (2000).

[6] J. Xu, C. I. Blaga, P. Agostini, and L. F. DiMauro, J. Phys. B: At. Mol. Opt. Phys. **49**, 112001 (2016).

[7] P. B. Corkum, Phys. Rev. Lett. **71**, 1994 (1993).

[8] M. Lewenstein, P. Balcou, M. Yu. Ivanov, A. L'Huillier, and P. B. Corkum, Phys. Rev. A **49**, 2117 (1994).

[9] S. V. Popruzhenko, J. Phys. B: At. Mol. Opt. Phys. **47**, 204001 (2014).

[10] T. Zuo, A. D. Bandrauk, and P. B. Corkum, Chem. Phys. Lett. **259**, 313 (1996).

[11] M. Ferray, A. L'Huillier, X. F. Li, L. A. Lompre, G. Mainfray, and C. Manus, J. Phys. B: At. Mol. Opt. Phys. **21**, L31 (1988).

[12] B. Walker, E. Mevel, B. Yang, P. Breger, J. P. Chambaret, A. Antonetti, L. F. DiMauro, and P. Agostini, Phys. Rev. A **48**, R894 (1993).

[13] M. Meckel, D. Comtois, D. Zeidler, A. Staudte, D. Pavičić, H. C. Bandulet, H. Pépin, J. C. Kieffer, R. Dörner, D. M. Villeneuve, and P. B. Corkum, Science **320**, 1478 (2008).

[14] M. G. Pullen, B. Wolter, A.-T. Le, M. Baudisch, M. Hemmer, A. Senftleben, C. D. Schröter, J. Ullrich, R. Moshammer, C. D. Lin, and J. Biegert, Nat. Commun. **6**, 7262 (2015).

[15] C. I. Blaga, J. Xu, A. D. DiChiara, E. Sistrunk, K. Zhang, P. Agostini, T. A. Miller, L. F. DiMauro, and C. D. Lin, Nature **483**, 194 (2012).

[16] M. Peters, T. T. Nguyen-Dang, E. Charron, A. Keller, and O. Atabek, Phys. Rev. A **85**, 053417 (2012).

[17] D. Zhong and A. H. Zewail, J. Phys. Chem. A **102**, 4031 (1998).

[18] W. Domcke and D. R. Yarkony, Annu. Rev. Phys. Chem. **63**, 325 (2012).

[19] C. Vozzi, M. Negro, F. Calegari, G. Sansone, M. Nisoli, S. De Silvestri, and S. Stagira, Nat. Phys. **7**, 822 (2011).

[20] J. Itatani, J. Levesque, D. Zeidler, H. Niikura, H. Pepin, J. C. Kieffer, P. B. Corkum, and D. M. Villeneuve, Nature **432**, 867 (2004).

[21] D. Pavičić, K. F. Lee, D. M. Rayner, P. B. Corkum, and D. M. Villeneuve, Phys. Rev. Lett. **98**, 243001 (2007).

[22] M. Peters, T. T. Nguyen-Dang, C. Cornaggia, S. Saugout, E. Charron, A. Keller, and O. Atabek, Phys. Rev. A **83**, 051403 (2011).

[23] C. Cornaggia, M. Schmidt, and D. Normand, J. Phys. B: At. Mol. Opt. Phys. **27**, L123 (1994).

[24] M. Elshakre, Int. J. Mass. Spectr. **336**, 37 (2013).

[25] Y. Sato, H. Kono, S. Koseki, and Y. Fujimura, J. Am. Chem. Soc. **125**, 8019 (2003).

[26] S. Chelkowski and A. D. Bandrauk, Int. J. Quantum Chem. **60**, 1685 (1996).

[27] L. Lehtovaara, J. Toivanen, and J. Eloranta, J. Comput. Phys. **221**, 148 (2007).

[28] A. Keller, Phys. Rev. A **52**, 1450 (1995).

[29] F. Krausz and M. Ivanov, Rev. Mod. Phys. **81**, 163 (2009).

[30] M. Spanner, O. Smirnova, P. B. Corkum, and M. Y. Ivanov, J. Phys. B: At. Mol. Opt. Phys **37**, L243 (2004).

[31] M. Meckel, A. Staudte, S. Patchkovskii, D. M. Villeneuve, P. B. Corkum, R. Dorner, and M. Spanner, Nat. Phys. **10**, 594 (2014).

[32] L. Chen, C. Huang, X. Zhu, P. Lan, and P. Lu, Opt. Express **22**, 20421 (2014).

[33] Y. Huismans, A. Rouzée, A. Gijsbertsen, J. H. Jungmann, A. S. Smolkowska, P. S. W. M. Logman, F. Lépine, C. Cauchy, S. Zamith, T. Marchenko, J. M. Bakker, G. Berden, B. Redlich, A. F. G. van der Meer, H. G. Muller, W. Vermin, K. J. Schafer, M. Spanner, M. Yu. Ivanov, O. Smirnova, D. Bauer, S. V. Popruzhenko, and M. J. J. Vrakking, Science **331**, 61 (2011).

[34] D. B. Milošević, G. G. Paulus, D. Bauer, and W. Becker, J. Phys. B: At. Mol. Opt. Phys, **39**, R203 (2006).

[35] M. Frasca, Proc. R. Soc. London A **463**, 2195 (2007).

[36] R. H. Reiss, in *Progress in Ultrafast Intense Laser Science III* (Springer, Berlin, 2008), pp. 1–31.

[37] D. B. Milošević, Phys. Rev. A **74**, 063404 (2006).

[38] N. D. Sengupta, Bull. Calcutta Math. Soc. **44**, 175 (1952).

[39] N. Suárez, A. Chacón, M. F. Ciappina, J. Biegert, and M. Lewenstein, Phys. Rev. A **92**, 063421 (2015).

[40] M. Busuladžić, A. Gazibegović-Busuladžić, D. B. Milošević, and W. Becker, Phys. Rev. A **78**, 033412 (2008).

[41] M. Yu. Ivanov, T. Brabec, and N. Burnett, Phys. Rev. A **54**, 742 (1996).

[42] K. Levenberg, Quart. Appl. Math. **2**, 164 (1944); D. W. Marquardt, J. Soc. Ind. Appl. Math. **11**, 431 (1963).